Helical thienothiophene (TT) and benzothieno-benzothiophene (BTBT) derivatives: synthesis, structural characterization and semiconducting properties

Maurizio Mastropasqua Talamo,[a] Flavia Pop,*[,a] Paul Hume,[c] Mamatimin Abbas,[b] Guillaume Wantz[b] and Narcis Avarvari,*[,a]

[a] Univ Angers, CNRS, MOLTECH-Anjou, SFR MATRIX, F-49000 Angers, France.

[b] Université de Bordeaux, IMS, CNRS, UMR-5218, Bordeaux INP, ENSCBP, Talence 33405, France.

[c] MacDiarmid Institute for Advanced Materials and Nanotechnology and School of Chemical and Physical Sciences, Victoria University of Wellington, Wellington, 6010, New Zealand

E-mail: flavia.pop@univ-angers.fr; narcis.avarvari@univ-angers.fr

Abstract

Thienothiophene (TT) and benzothieno-benzothiophene (BTBT) have been successfully included here in the helical backbone of helicene derivatives. The employed synthetic approach gives access in a controlled manner to both simple and double helicenic structures decorated with side alkyl chains to provide solubility. Whereas in the solid state structure the *M* and *P* forms of the mono-helicene stack in alternated rows of each enantiomer and show segregation between the aromatic and aliphatic parts, the crystal of the bis-helicene is formed of homochiral sheets of *MM* and *PP* enantiomers. These helical TT and BTBT materials have been tested as racemic mixtures in organic field-effect transistors (OFETs) devices fabricated by both spin coating and vapour deposition. The bis-helicene derivative, which crystal packing is dominated by π-π stacking interactions, behaves as p-type semiconductor with a hole mobility of 3.5×10^{-5} cm^2 V^{-1} s^{-1} in close agreement with the predicted value by DFT calculations. The OFETs of mono-helicene do not show charge transport despite the superior predicted mobility based on the crystal structure, suggesting that amorphous films suffer from a broader distribution of hole energies, which limits the number of thermally accessible hopping pathways. The benefits of embedding TT and BTBT units into helicenic structures in terms of synthetic strategy, structural variation and mobility, pave the way towards chiral semiconducting BTBT helicenes.

1. Introduction

Molecular organic semiconductors (OSCs) have been largely utilized in a range of different advanced optoelectronic technologies, making use of their particular features such as light absorption and/or emission, and charge transport properties that can be tuned by chemical synthesis.[1, 2]

Chalcogen-containing heteroacenes are a class of molecular organic semiconductors that have been developed to accomplish charge transport functions such as active layers in organic field-effect transistors (OFETs).[3] In particular, derivatives of the [1]benzothieno[3,2-*b*]benzothiophene (BTBT) have shown p-type semiconducting properties with outstanding hole mobility up to 43 $cm^2\ V^{-1}\ s^{-1}$ in OFETs devices fabricated by convenient solution techniques.[4] The cornerstone of the success of BTBT and its derivatives lies in an effective charge delocalization across a compact molecular structure, and a good crystallinity dominated by π-π stacking and chalcogen interactions.[5]

The introduction of chirality into the molecular structure of organic semiconductors has been thought as an expedient strategy to access new functions such as chiral molecular recognition,[6] enantioselective electrochemistry,[7,8] circularly polarized luminescence (CPL)[9] and CPL detection,[10,11] and the development of spintronic applications.[12] This concept recently fostered a growing interest into chiral organic semiconductors such as helicene derivatives[8,10,11,13] and chiral perovskites.[14] Despite the leading role of BTBT as p-type semiconductor, examples of chiral BTBT derivatives are scarce in literature and not fully explored as chiral semiconductors.[15,16] Note, for example, that very recently Takimiya et al. have described enantiopure dinaphtho[2,3-b:20,30-f]thieno[3,2-b]thiophene (DNTT) containing 2-ethylhexyl chains, yet no differences in performances of thin-film OFETs have been observed between the enantiopure and racemic materials.[17] The authors thus hypothesized that the intermolecular interactions between the planar DNTT cores are much stronger than those involving the 2-ethylhexyl groups, therefore the former should predominantly contribute to the crystallization process during thin-film formation. In this respect, alternative sources of molecular chirality, other than point chirality on the alkyl side chains, situated especially on the aromatic portion of thienoacene semiconductors, are worth to be explored, including the inherent helical chirality of helicene-like molecules. Indeed, while various extended BTBTs with planar structures are known, to the best of our knowledge no example of extended BTBT embedded in helical backbones have ever been reported to date. The deformation of the π-system should help for an effective coupling between charge carriers and chiroptical properties, although it could be detrimental to the semiconducting properties due to a looser molecular packing in the crystal. In this study we aimed to develop helical extended BTBTs in order to assess whether the introduction of BTBT motifs is beneficial to the semiconducting properties of helicene derivatives as a first step towards larger families of helicene-BTBTs as chiral semiconductors.

2. Results and discussion

2.1 Synthesis and crystal structures of the helical BTBTs

The synthesis of symmetric extended BTBTs usually follows the well-established pathway based on the iodine-promoted cyclization of *o*-bis(methylthio)stilbene precursors.[18] Alternative strategies accessing unsymmetrical extended BTBTs are possible, involving consecutive thienannulation reactions starting from readily available *o*-ethynylthio-anisoles,[19] or benzannulation reactions starting from thieno[3,2-*b*]thiophene (**TT**).[20] On account of the commercial availability of the starting material **TT** we aimed to gain a further insight on its synthetic potentiality towards helical **BTBT** derivatives. Formyl and acyl functions can be easily introduced at the positions 2 (unsymmetrically) or 2,5 (symmetrically) of **TT**, providing access to multiple **TT** carbonyl derivatives, which in turn can be converted into stilbene-like derivatives by Wittig olefination.[21-24] These precursors can finally yield, in principle, **TT**-fused helicenes through oxidative photocyclization reactions.

Scheme 1 Synthetic route towards the helicene-TT and helicene-BTBT compounds **4** and **5**, respectively.

In order to introduce solubilizing chains we performed a Friedel-Crafts acylation which afforded the diacylated compound **1**. The carbonyl functions of **1** were olefinated with the (naphthalen-2-ylmethyl)triphenylphosphonium bromide under Wittig condition in presence of *n*BuLi as the base. By controlling the stoichiometry of *n*Buli and phosphonium reagent it was possible to direct the Wittig reaction toward the mono- or bis-stilbene-like derivatives, **2** and **3** respectively, as mixtures of *E* and *Z* isomers. Finally, the oxidative photocyclization of **2** and **3** yielded the helicenic compounds **4** and **5** (Scheme 1). Interestingly, this strategy not only gives smooth access to soluble helicene-BTBT derivatives, but also allows the introduction of alkyl substituents with unusual regioselectivity at the 1 and 6 positions of the BTBT core.[25]

The structures of **4** and **5** were unambiguously confirmed by single crystal X-ray analysis, which clearly showed the helical conformation within the phenanthro[3,4-b]thieno[2,3-d]thiophene (**PTT**) portion of the molecule. Compound **4** crystallizes as a racemate in the triclinic system, space group *P*–1, with two independent molecules in the asymmetric unit. The crystal packing features a clear segregation between the alkyl chains and the aromatic rings. The molecules align along the *b* axis, forming rows of *MM* enantiomers alternating in

the *a* direction with offset rows of *PP* enantiomers. The enantiomers of the adjacent rows are interacting through two distinct S···S contacts, and H-bonds with sulfur and oxygen as the acceptors (Fig. 1, Figs. S1-S2, Tables S1-S2).

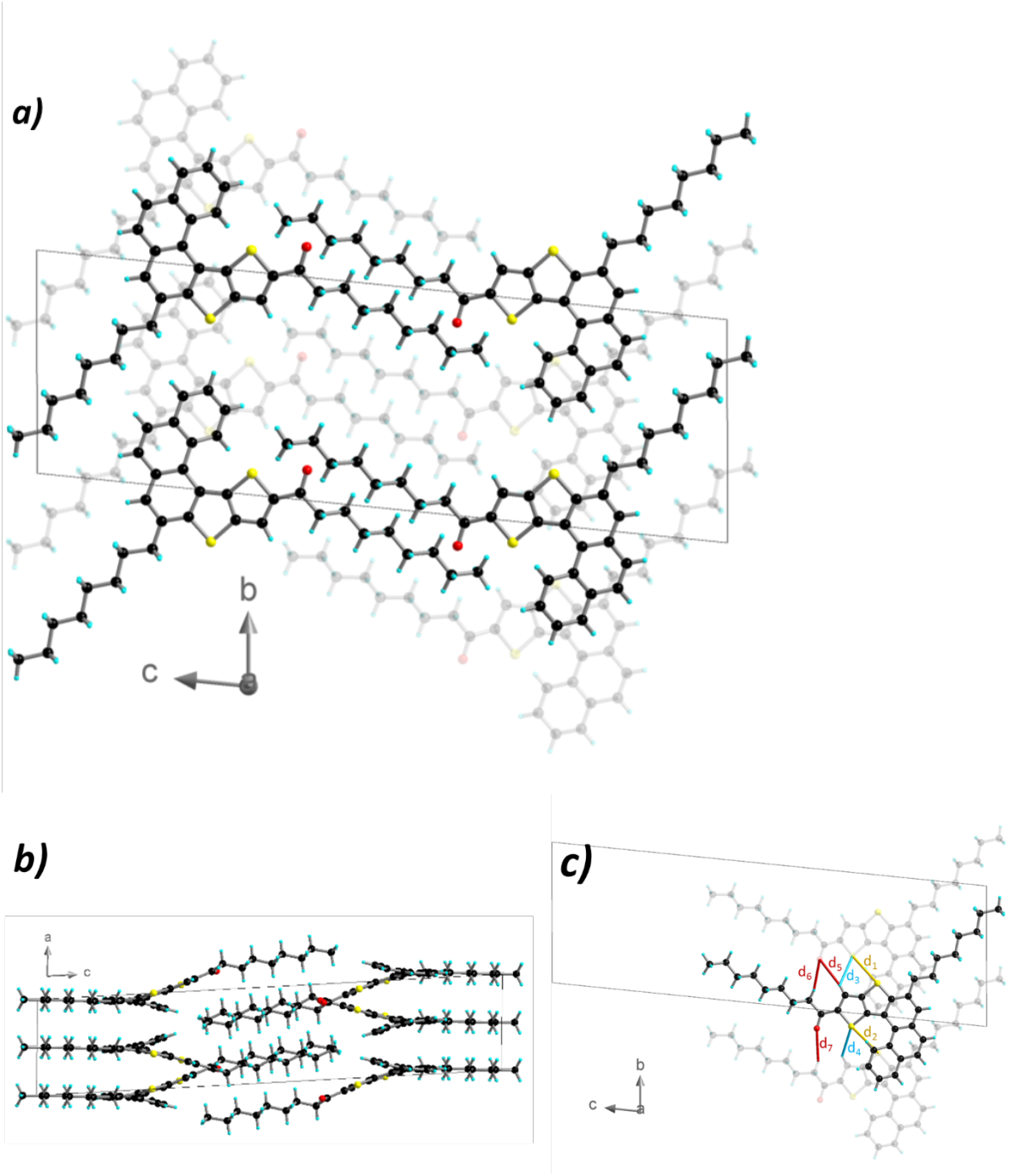

Fig. *1* Crystal packing of compound **4**. View along a) a axis and b) b axis. In c) intermolecular contacts are highlighted in yellow for S···S, blue for S···H and red for O···H, with distances equal to $d_1 = 3.54$ Å, $d_2 = 3.89$ Å, $d_3 = 2.87$ Å, $d_4 = 2.86$ Å, $d_5 = 2.67$ Å, $d_6 = 2.58$ Å, and $d_7 = 2.73$ Å.

Due to the presence of the two stereogenic helicene motifs within the compound **5**, the molecule can exist as three different stereoisomers - namely *MM*, *PP* and *meso*; however, in the crystal, the compound **5** adopts only the enantiomeric *MM* and *PP* configurations, with racemic composition (Fig. 2, Fig. S3, Tables S3-S4). The resulting phase pertains to the monoclinic system, space group $P2_1/n$, with one independent molecule in the asymmetric unit. Contrary to the expectations,

the crystal packing does not showcase intermolecular S···S interactions, however π-π interactions with distances in the range 3.5 – 3.7 Å have been observed. The molecules are arranged into homochiral sheets stacking along the *b* direction with a repetition pattern *MM-PP*-(*MM*)'-(*PP*)'. Within each sheet the molecules organize into staggered rows aligned along the *a* axis and held together by hydrophobic forces. The stacking along *b* occurs with an offset that cause the thienothiophene (**TT**) cores to overlap the alkyl chains of the sheet below. Along the *b* direction, it is also possible to observe the formation of *MM-PP* dimers through a perfectly aligned π-stacking (eclipsed aromatic units corresponding to a stacking angle close to 90°) of the terminal rings.

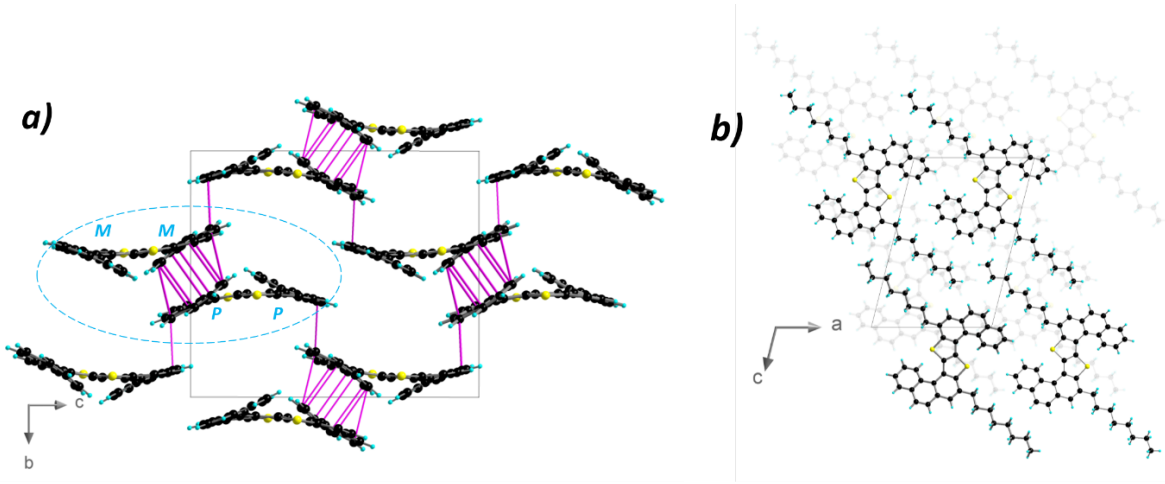

Fig. *2* Crystal packing of compound **5**. a) View along a axis (alkyl chains omitted for clarity), with MM-PP dimers circled in light blue, and contacts between sp^2 carbons (3.5 Å < d < 3.7 Å) highlighted in purple. b) View along the b axis.

The redox potential of molecules **4** and **5** have been investigated by cyclic voltammetry (Fig. S4). While compound **4** showed an irreversible oxidation peak at 1.51 V vs. SCE, the compound **5** revealed a reversible redox system with $E_{1/2}$ = 1.30 V vs. SCE, which is close to previously found values (1.31 V vs. SCE) in similar binaphthothieno-thiophene derivatives.[26]

2.2 Field-effect characteristics of thin films of helical TT 4 and BTBT 5

Homogeneous thin films of **4** and **5** were deposited by spin coating and by vapour deposition onto n-doped silicon with 200 nm thermally grown oxide (Figs. S5-S9). In the first case, solutions in chlorobenzene (70 µL, 10 mg/mL) of compounds **4** and **5** were spin casted (90 s at 1000 rpm) onto substrates modified with a poly(1-vinyl-1,2,4-triazole) (PVT) passivation layer,[27] and finally annealed for 1 h at 50 °C to remove the trace solvents. In the second case, 25 nm layers were deposited at a rate of 1 nm/min onto substrates modified with a polystyrene (PS) passivation layer. OFETs devices were finally fabricated by thermal evaporation of top-contact electrodes (10 nm MoO_3, 70 nm Ag) through shadow masks with channels of 1 mm width and 50 µm length (*W/L* = 20). This electrode combination was chosen as it was proven the best one for C_8-BTBT

devices.[28] The devices were annealed for 15 min at 100 °C to further optimize the electrode and active layer interface. Optical microscopy under polarized light showed regular crystalline domains with sizes in the order of 10 µm for compound **5** (Figs. 3a and 3c, Figs. S8-S9), whereas compound **4** displayed much smaller crystal sizes (Figs. S5-S7). Finally, while compound **4** failed to show any measurable charge transport, **5**-based OFETs exhibited p-type FET characteristics with current on/off ratio in the order of 10^4 (Fig. 3b and 3d). Square root of the drain current (I_{ds}) curves both deviated from linearity at high gate voltage region, suggesting the presence of strong contact resistance at the interface. Therefore, this part of the curve was avoided in deriving the mobility of the devices, in order to minimize device related factors. A slight difference was observed for spin coated and vapour deposited devices. μ_h^{sat} of spin coated device was $1{,}7*10^{-5}$ cm^2 V^{-1} s^{-1}, while a slightly higher mobility of $3{,}5*10^{-5}$ cm^2 V^{-1} s^{-1} was achieved for the vapour deposited device. Indeed, microscope images showed larger and denser crystal domains for vapour deposited films, which is preferable for charge transport. It is worth mentioning that OFETs mobilities are strongly dependant on film morphology and device structure, and that single crystal devices with optimum interface would be more suitable to infer intrinsic semiconductor mobilities.[29]

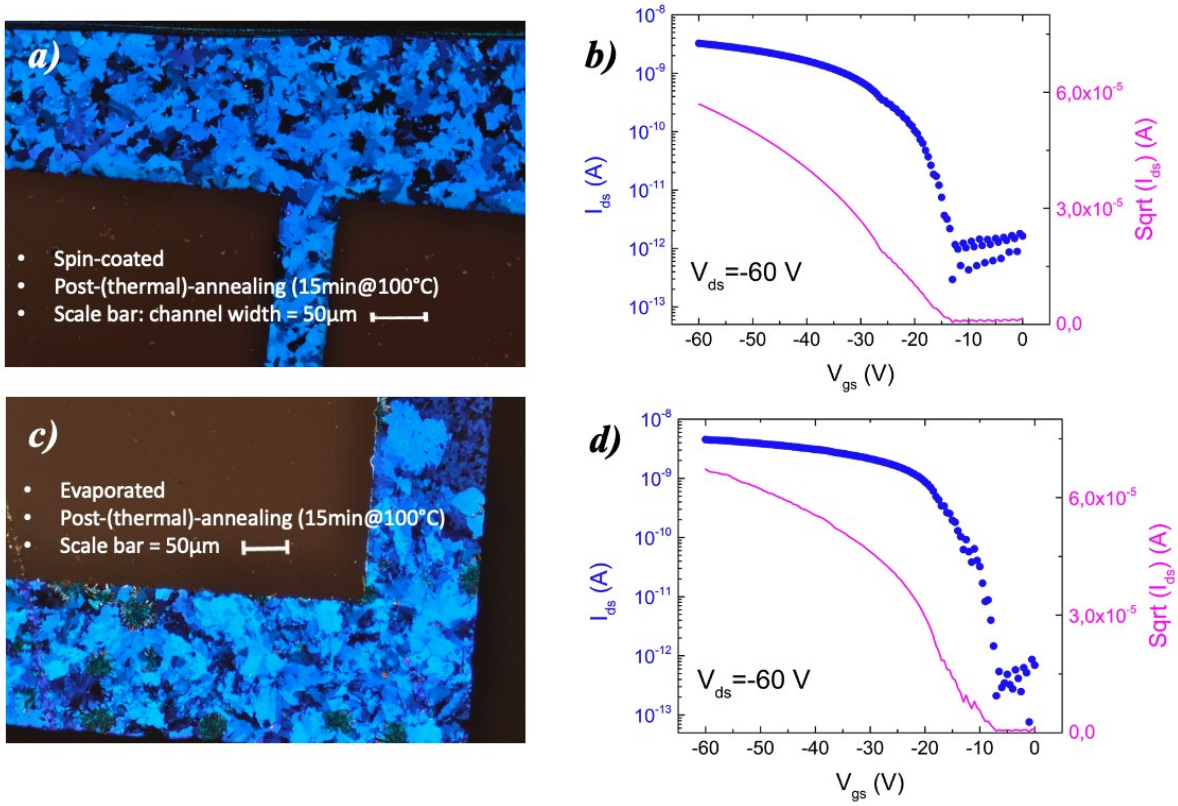

Fig. *3* Micrographs under cross-polarized light of the OFETs devices based on **a)** spin-coated and **c)** vapour deposited organic layers, with the corresponding OFETs transfer characteristic **b)** and **d)** for the spin-coated and vapour deposited semiconductor **5**, respectively.

2.3 Crystallographic characterisation of the films

The OSC film structures were studied by X-ray diffraction (XRD) in the interval $5° < 2\theta < 25°$, and the experimental diffraction patterns were compared with simulated powder diffraction patterns generated from the corresponding single

crystal structures (Fig. S10). On this purpose, films of **4** and **5** were deposited by vapour deposition and by spin-coating onto glass slides modified with PS and PVT coating, respectively. The layers of compound **4** deposited by vapour deposition showed diffraction peaks at 2θ = 7.34° (*d*-spacing = 1.20 nm), 2θ = 11.00° (*d*-spacing = 0.80 nm), 2θ = 18.37° (*d*-spacing = 0.48 nm), and higher orders at 2θ = 14.66° (*d*-spacing = 0.60 nm) and 2θ = 22.07° (*d*-spacing = 0.40 nm) that do not evolve upon annealing. These peaks do not match those predicted for the single crystal phase obtained for compound **4**. However, when deposited by spin coating, films of **4** show before annealing a different diffraction pattern with peaks at 7.5° (*d*-spacing = 1.19 nm), 9.79° (*d*-spacing = 0.90 nm) and 12.26° (*d*-spacing = 0.72 nm) that match the planes [0 0 -3], [0 0 -4] and [0 0 -5] of the single crystal phase, respectively. This indicates the formation of crystallites with the same structure as the single crystal, highly oriented with the *a* and *b* axes parallel to the substrate. In this organization, the stacking direction is parallel to the substrate, and the alkyl chains point towards the substrate (edge-on). Despite this is generally considered the optimal configuration for the charge transport, the crystal domains are very likely too small to sustain an effective charge transport during the transistor operation. Unfortunately, as shown by XRD analyses, the thermal annealing (under the experimental conditions previously described in paragraph 2.2) does not increase the size of the crystal domains. Rather, a phase transition occurs producing the same phase as for the vapour deposited film, whose structure is unknown. Little we can say about the semiconducting properties of this latter phase, except that according to the micrographs under cross-polarised light (Fig. S6 and S7) the morphology shows a high fragmentation, and therefore the charge transport is expected to be heavily affected by defects, irrespective of the intrinsic properties of the crystal phase.

Conversely, compound **5** did not show polymorphism between the single crystal phase, the vapour deposited and the spin-casted films before and after annealing. XRD analyses on vapour deposited films clearly show two peaks at 2θ = 9.80° (*d*-spacing = 0.90 nm) and 2θ = 14.75° (*d*-spacing = 0.60 nm) that match the planes [0 0 2] and [-1 0 3] of the single crystal phase, respectively (Fig. 4). The *k* index equal to 0 indicates again a preferential orientation of the crystallites with the *b* axis parallel to the substrate. However in this case the molecules adopt both the edge-on (alkyl chains perpendicular to the substrate) and end-on (alkyl chains parallel to the substrate) orientation, which can produce trap-sites localised at the grain boundaries. On the other hand, spin-casted films initially show a peak at 2θ = 7.52° (*d*-spacing = 1.18 nm) which match the plane [-1 0 1] of the single crystal phase. Once again, the *b* axis is parallel to the substrate, with the molecules adopting an end-on orientation (Figs. S11-S13). After annealing, the peaks corresponding to the [0 0 2] and [-1 0 3] appear, indicating a gradual reorientation of the crystallites toward the edge-on alignment.

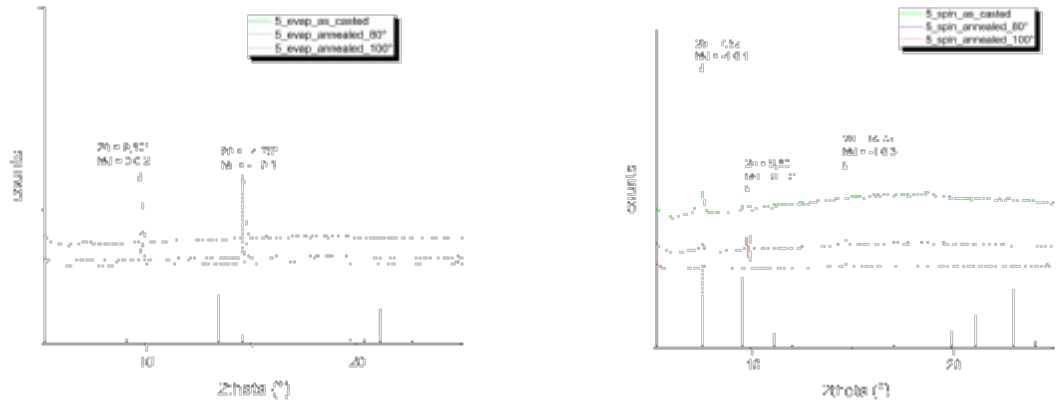

Fig. 4 X-ray diffraction patterns from vapour deposited (left) and spin-casted (right) films of compound **5**: as deposited (green line), after 10 min at 80 °C (violet line), after 10 min at 100 °C (red line), and theoretical isotropic powder diffraction (black histogram).

Note that both compounds show excellent thermal stability according to DSC and TGA analyses (Figs. S14-S17).

2.4 DFT predicted hole mobilities

To gain insight into the photophysical behaviour of **4** and **5**, we performed density functional theory (DFT) calculations based on the crystal structures, which we used to estimate mobilities for hole transport (Tables S5-S6). The predicted value of μ_h = 1.0 × 10^{-4} cm^2 V^{-1} s^{-1} for compound **5** is in close agreement with the mobility extracted from our OFETs devices (3.5 × 10^{-5} cm^2 V^{-1} s^{-1}). Interestingly, the predicted mobility for **4** is significantly larger (μ_h = 8.5 × 10^{-3} cm^2 V^{-1} s^{-1}), due to a combination of lower reorganisation energy (λ = 0.37 eV for **4** vs 0.70 eV for **5**) and stronger electronic couplings V (maximum $|V|$ = 22.5 meV for **4** *vs* 9.3 meV for **5**). This suggests that the reason for the lower experimental mobility of **4** is likely to be morphological in origin, such as the small crystal domains observed in the film XRD measurements (which limit the long-range mobility via grain boundaries). Films of **4** may also possess larger energetic disorder compared to those of **5** (i.e. a broader distribution of hole energies, limiting the number of thermally accessible hopping pathways). This would be expected from the Bässler model, due to larger dipole moment of **4** compared to **5** (3.8 D vs 0.6 D, respectively).[30-32]

3. Conclusion

We reported here the first synthesis of a BTBT derivative with helical molecular structure, obtained in three straightforward steps from commercially available thieno[3,2-*b*]thiophene. This synthetic strategy allows the introduction of alkyl chains for solubilisation purposes, with an uncommon specificity at the positions 1 and 6 of the BTBT core, providing the accessibility of the correspondent alkyl-carboxylic acids or acyl chlorides precursors. The same method allows the obtainment of a thienothiophene derivative fused with a phenanthreno group, which gives a helicene of five rings. Despite the lack of sizeable semiconducting properties, this molecule provides a nonanoyl group available for further functionalization and/or annulation. The crystallographic analysis of the symmetrical extended BTBT **5** shows an uncommon aligned sandwich

configuration in the π-stacking between the terminal benzo rings, yet no interactions between the sulfur atoms were observed. Molecule **5** behaves as a p-type semiconductor in OTFT with mobilities reaching up $3.5*10^{-5}$ cm^2 V^{-1} s^{-1} which approach those observed in azahelicene films.[10] However these latter were recorded on enantiopure materials while our platform is racemic. Since it is known that the enantiomeric composition can dramatically affect the semiconducting properties,[33-36] further work will be devoted to the preparation of enantiopure BTBTs containing configurationally stable helicene units and to the introduction of chiral chains.

4. Experimental

4.1 Materials and methods

All commercially available reagents and solvents were used as received unless otherwise noted. Dry tetrahydrofuran was directly used from the purification machines. Chloroform as solvent for synthesis was distilled over calcium hydride prior to use. Chromatography purifications were performed on silica gel Sorbent Technologies Silica Gel (60 Å, 65 x 250 mesh) and thin layer chromatography (TLC) was carried out using aluminum sheets precoated with silica gel 60 (EMD 40−60 mm, 230−400 mesh with 254 nm dye). All reactions were carried out in Schlenk tubes under argon atmosphere. Dropwise additions were done with a programmable syringe pump. NMR spectra were acquired on a Bruker Avance DRX 300 and 500 spectrometers operating at 300 and 500 MHz for ^{1}H and 75 and 125 MHz for ^{13}C, respectively, at room temperature in $CDCl_3$ solutions. ^{1}H and ^{13}C NMR spectra were referenced to the residual protonated solvent (^{1}H) or the solvent itself (^{13}C). All chemical shifts are expressed in parts per million (ppm) downfield from external tetramethylsilane (TMS), using the solvent residual signal as an internal standard and the coupling constant values (J) are reported in Hertz (Hz). The following abbreviations have been used: s, singlet; dd, doublet of doublets; m, multiplet. Mass spectrometry MALDI–TOF MS spectra were recorded on Bruker Biflex-IIITM apparatus, equipped with a 337-nm N_2 laser.
Powder and film X-ray diffraction (XRD) experiments were performed on a Bruker D8 Advance diffractometer (θ/2θ reflection mode) equipped with a Lynxeye detector and CuKα radiation (λ = 1.5406 Å). DSC measurements were recorded on a Differential Scanning Calorimeter DSC Q20, TA Instruments. TGA measurements were recorded on a Thermogravimetric analyser TGA Q500, TA Instruments.

4.2 Synthesis

Synthesis of 1,1'-(thieno[3,2-*b*]thiophene-2,5-diyl)bis(nonan-1-one) (1). Nonanoic acid (1 mL, 5.71 mmol, 2 eq.) was dissolved into DCM (10 mL) under argon atmosphere, then oxalyl chloride (0.54 mL, 6.28 mmol, 2.2 eq.) and few drops of DMF were added. The resulting mixture was stirred for 1 h at r.t., then volatile components were removed at the rotary evaporator. The reaction vessel was reconditioned with 2 cycles of vacuum/argon. At 0 °C, thieno[3,2-*b*]thiophene (0.400 g, 2.85 mmol, 1eq.) and $AlCl_3$ (1.52 g, 11.41 mmol, 4 eq.) were added, and the mixture further stirred at r.t. overnight. The reaction was quenched by carefully adding water, extracted into DCM and washed with brine. The organic

layer was dried over anhydrous $MgSO_4$ and the solvent removed under reduced pressure. The crude was dissolved into a minimum quantity of DCM then pentane was added in small portion to precipitate the product **1** that was eventually collected by filtration. The filtrate was evaporated and purified by column chromatography on silica gel (DCM/AcOEt 95:5 as the eluent) affording some more compound **1**. The compound **1** was obtained with an overall yield of 66% (0.796 g) as a white solid (m.p. = 132 °C).

^{1}H NMR (300 MHz, $CDCl_3$) δ 7.89 (s, 2H), 2.94 (t, *J* = 7.5 Hz, 4H), 1.77 (p, *J* = 7.5 Hz, 4H), 1.31 (m, 20H), 0.88 (t, *J* = 6.8 Hz, 6H) ppm.

^{13}C NMR (76 MHz, $CDCl_3$) δ 194.19, 149.77, 143.78, 124.41, 39.40, 31.96, 29.52, 29.47, 29.28, 24.88, 22.79, 14.25 ppm.

HRMS (without matrix, MH+) calcd for $C_{24}H_{37}O_2S_2^+$ 421.22295; found 421.22284.

Synthesis of 1-(5-(1-(naphthalen-2-yl)dec-1-en-2-yl)thieno[3,2-b]thiophen-2-yl)nonan-1-one (2). In a round bottom flask (naphthalen-2-ylmethyl)triphenylphosphonium bromide[37] was dissolved (0.350 g, 0.72 mmol, 1 eq) in dry THF (10 mL). At -78 °C, *n*-BuLi (0.45 mL, 0.72 mmol, 1.6 M in hexane, 1 eq) was slowly added and the mixture turned from white to red. The mixture was allowed to reach the r.t. in 15 min and stirred for additional 10 min. The mixture was then cooled down at -78 °C and **1** (0.305 g, 0.72 mmol, 1 eq) was added. The mixture was allowed to reach the r.t. and then refluxed under stirring overnight. The mixture was filtered through a celite pad and rinsed with THF. After evaporation of the solvent, the crude was purified by column chromatography on silica gel (PE/DCM 7:3 as the eluent), affording 0.280 g (71% yield) of **2** as a yellowish solid containing a mixture 1.3:1 of *E*/*Z* isomers.

^{1}H NMR (300 MHz, $CDCl_3$) δ 7.90 – 7.83 (m, $5H_E$ = 6.5H), 7.80 – 7.72 (m, $3H_Z$ = 3H), 7.70 (s, $1H_Z$ = 1.3H), 7.65 (d, J = 8.6 Hz, $1H_Z$ = 1H), 7.55 – 7.44 (m, $2H_Z$ + $3H_E$ = 5.9H), 7.36 (s, $1H_E$ = 1.3H), 7.26 (dd, J = 8.6, 1.6 Hz, $1H_Z$ = 1H), 7.19 (s, $1H_E$ = 1.3H), 7.09 (s, $1H_Z$ = 1H), 6.81 (s, $1H_Z$ = 1H), 2.97 – 2.91 (t, J = 7.35 Hz, $2H_E$ = 2.6H), 2.93 – 2.87 (t, J = 7.35 Hz, $2H_Z$ = 2H), 2.85 – 2.76 (t, J = 8.10 Hz, $2H_E$ = 2.6H), 2.63 (t, J = 7.4 Hz, $2H_Z$ = 2H), 1.80 (m, $4H_Z$ + $2H_E$ = 6.6H), 1.68 – 1.55 (m, $2H_E$ = 2.6H), 1.37 (m, $20H_Z$ + $20H_E$ = 46H), 0.93 (m, $6H_Z$ + $6H_E$ = 13.8H) ppm.

^{13}C NMR (76 MHz, $CDCl_3$) δ 193.96, 193.89, 154.49, 150.25, 145.48, 145.29, 145.22, 144.68, 138.96, 137.48, 137.07, 135.70, 134.57, 134.44, 133.44, 133.41, 132.51, 129.89, 128.75, 128.47, 128.11, 127.99, 127.98, 127.88, 127.68, 127.64, 127.02, 126.94, 126.37, 126.22, 126.11, 126.05, 124.37, 119.24, 116.26, 40.53, 39.11, 39.07, 31.92, 30.80, 29.87, 29.47, 29.44, 29.33, 29.26, 29.22, 29.20, 28.62, 25.11, 22.71, 14.16 ppm.

HRMS (DCTB, M+) calcd for $C_{35}H_{44}OS_2^+$ 544.28281; found 544.28119 .

Synthesis of 3,6-bis(1-(naphthalen-2-yl)dec-1-en-2-yl)thieno[3,2-b]thiophene (3). In a round bottom flask (naphthalen-2-ylmethyl)triphenylphosphonium bromide[37] was dissolved (1.160 g, 2.4 mmol, 2 eq) in dry THF (20 mL). At -78 °C, *n*-BuLi (0.96 mL, 2.4 mmol, 1.6 M in hexane, 2 eq) was slowly added and the mixture turned from white to red. The mixture was allowed to reach the r.t. in 15 min and stirred for additional 10 min. The mixture was then cooled down at -78 °C and **1** (0.500 g, 1.2 mmol, 1 eq) was added. The

mixture was slowly allowed to reach the r.t. and then refluxed under stirring overnight. The mixture was filtered through a celite pad and rinsed with THF. After evaporation of the solvent, the crude was purified by column chromatography on silica gel (PE/DCM 9:1 as the eluent) affording 0.316 g (40 % yield) of **3** as a yellowish solid containing a mixture 0.2:1:0.04 of *EE/EZ/ZZ* isomers.

^{1}H NMR (300 MHz, $CDCl_3$) δ 7.99 – 6.64 (m, $18H_{EE}$ + $18H_{ZE}$ + $18H_{ZZ}$ = 22.3H), 2.97 – 2.74 (m, $2H_{EE}$ + $2H_{ZE}$ = 2.4H), 2.73 – 2.59 (m, $2H_{ZE}$ + $2H_{ZZ}$ = 2.04H), 1.96 – 1.72 (m, $2H_{EE}$ + $2H_{ZE}$ = 2.4H), 1.74 – 1.60 (m, $2H_{ZE}$ + $2H_{ZZ}$ = 2.04H), 1.59 – 1.27 (m, $20H_{EE}$ + $20H_{ZE}$ + $20H_{ZZ}$ = 24.8H), 1.03 – 0.93 (m, $6H_{EE}$ + $6H_{ZE}$ + $6H_{ZZ}$ = 7.4H) ppm.

^{13}C NMR (76 MHz, $CDCl^3$) δ 149.53, 149.17, 148.90, 148.60, 145.06, 144.82, 144.60, 144.26, 139.63, 139.14, 138.91, 138.20, 137.54, 137.47, 137.00, 136.25, 135.21, 135.19, 135.00, 134.96, 133.59, 133.54, 133.52, 133.49, 132.51, 132.48, 132.39, 132.36, 128.52, 128.41, 128.11, 128.09, 128.02, 127.99, 127.91, 127.88, 127.69, 127.60, 127.56, 127.28, 126.64, 126.53, 126.28, 126.27, 126.01, 125.97, 125.87, 119.08, 119.01, 118.88, 118.75, 116.17, 116.09, 115.96, 115.80, 40.94, 40.88, 40.75, 40.64, 39.63, 39.41, 31.98, 31.96, 30.87, 30.80, 29.98, 29.68, 29.55, 29.40, 29.31, 28.81, 22.79, 14.24 ppm.

HRMS (DCTB, M+) calcd for $C_{46}H_{52}S_2^+$ 668.35049; found 668.35223 .

Synthesis of 1-(8-octylphenanthro[3,4-b]thieno[2,3-d]thiophen-11-yl)nonan-1-one (4). A mixture of *E/Z* isomers of the compound **2** (0.580 g, 1.06 mmol, 1eq) and I_2 (0.270 g, 1.06 mmol, 1 eq) were dissolved in toluene (650 mL). Argon was bubbled through the solution for 15 min, and then propylene oxide (3.7 mL, 53.23 mmol, 50 eq) was added to the mixture. The mixture was stirred and irradiated overnight with a Hg lamp (150 W). After the evaporation of the solvent, the crude was purified by column chromatography on silica gel (PE/DCM 6:4 as the eluent), and recrystallization from hot MeOH affording 0.400 g (69 % yield) of **4** as white crystals (m.p. = 73 °C).

^{1}H NMR (300 MHz, $CDCl_3$) δ 9.23 (dd, *J* = 8.1, 0.8 Hz, 1H), 8.02 (s, *J* = 1.7 Hz, 1H), 7.99 (dd, *J* = 7.8, 1.4 Hz, 1H), 7.84 (d, *J* = 8.5 Hz, 1H), 7.80 (s, *J* = 8.7 Hz, 1H), 7.75 (ddd, *J* = 8.3, 4.9, 1.7 Hz, 1H), 7.72 – 7.66 (m, 1H), 7.68 (s, 1H), 3.05 (d, *J* = 7.5 Hz, 2H), 2.98 (d, *J* = 7.8 Hz, 2H), 1.91 (p, *J* = 7.5 Hz, 2H), 1.81 (p, *J* = 7.5 Hz, 2H), 1.52 – 1.25 (m, 20H), 0.92 – 0.85 (m, 7H) ppm.

^{13}C NMR (76 MHz, $CDCl_3$) δ 194.28, 145.97, 143.13, 142.88, 138.82, 136.57, 132.65, 131.46, 129.09, 128.38, 127.16, 127.12, 126.85, 126.65, 125.81, 125.65, 125.63, 124.21, 39.47, 34.81, 32.03, 31.99, 31.06, 29.77, 29.60, 29.56, 29.39, 29.31, 25.15, 22.81, 14.24 ppm.

HRMS (DCTB, M^+) calcd for $C_{35}H_{42}OS_2^+$ 542.26716; found 542.26829.

Synthesis of 8,17-dioctylphenanthro[4,3-b]phenanthro[3',4':4,5]thieno[2,3-d]thiophene (5). The mixture of *EE/EZ/ZZ* isomers of the compound **3** (0.360 g, 0.54 mmol, 1 eq) and I_2 (0.273 g, 1.08 mmol, 2 eq) were dissolved in toluene (650 mL). Argon was bubbled through the solution for 15 min, and then propylene oxide (3.8 mL, 53.81 mmol, 100 eq) was added to the mixture. The mixture was stirred and irradiated overnight with a Hg lamp (150 W). After the evaporation of the solvent, the crude was purified by column chromatography on silica gel (PE/DCM, 9:1 as the eluent) affording 0.250 g (70 % yield) of **5** as white crystals (m.p. = 142 °C).

^{1}H NMR (300 MHz, $CDCl_3$) δ 9.49 (dd, J = 8.1, 0.8 Hz, 2H), 8.05 (dd, J = 7.8, 1.3 Hz, 2H), 7.87 (d, J = 8.7 Hz, 2H), 7.82 (d, J = 8.7 Hz, 2H), 7.80 (td, J = 7.2, 1.5 Hz, 2H), 7.74 (td, J = 6.9, 1.5 Hz, 2H), 7.66 (s, 2H), 3.05 (d, J = 7.8 Hz, 4H), 1.93 (d, J = 7.2 Hz, 4H), 1.51 – 1.26 (m, 20H), 0.88 (d, J = 6.7 Hz, 6H) ppm.

^{13}C NMR (76 MHz, $CDCl_3$) δ 140.50, 137.47, 136.22, 132.59, 131.48, 129.11, 128.98, 128.34, 127.11, 127.02, 126.85, 126.74, 125.36, 125.12, 124.67, 34.29, 32.05, 29.73, 29.61, 29.40, 29.35, 22.82, 14.26 ppm.

HRMS (DCTB, M+) calcd for $C_{46}H_{48}S_2^+$ 664.31919; found 664.31765.

4.3 X-Ray structure determinations

Details about data collection and solution refinement are given in Table 1. Single crystals of the compounds were mounted on glass fibre loops using a viscous hydrocarbon oil to coat the crystal and then transferred directly to cold nitrogen stream for data collection. X-ray data collection were performed at 150 K and ambient temperature on an Agilent Supernova with CuKα (λ = 1.54184 Å). The structures were solved by direct methods with the SHELXS-97 and SIR92 programs and refined against all F^2 values with the SHELXL-97 program using the WinGX graphical user interface. All non-H atoms were refined anisotropically. Hydrogen atoms were introduced at calculated positions (riding model), included in structure factor calculations but not refined. Crystallographic data for the two structures have been deposited with the Cambridge Crystallographic Data Centre, deposition numbers CCDC 2153711 (**4**) and CCDC 2153712 (**5**). These data can be obtained free of charge from CCDC, 12 Union road, Cambridge CB2 1EZ, UK (e-mail: deposit@ccdc.cam.ac.uk or http://www.ccdc.cam.ac.uk).

Table 1 Detailed crystallographic data.

	4	**5**
Chemical formula	$2*(C_{35}H_{42}OS_2)$	$C_{46}H_{48}S_2$
M_r	542.81	664.96
Crystal system, space group	Triclinic, *P*-1	Monoclinic, $P2_1/n$
Temperature (K)	150 K	296 K
a, *b*, *c* (Å)	7.3136(5), 11.4786(6), 35.7537(13)	12.9341(5), 15.4930(7), 18.7811(8)
α, β, γ (°)	83.861(4), 85.675(4), 86.150(5)	90, 104.190(4), 90
V (Å^3)	2970.5(3)	3648.7(3)
Z	2	4
ρ_{calc} (g.cm^{-3})	1.214	1.211
μ (Cu *K*α) (mm^{-1})	1.807	1.547
No. of measured, independent and observed [$I > 2\sigma(I)$] reflections	22721, 11149, 7163	16021, 7005, 5269
R_{int}	0.0788	0.0294
$R[F^2 > 2\sigma(F^2)]$, $wR(F^2)$, *S*	0.0925, 0.2428, 1.059	0.0625, 0.1933, 1.061
CCDC number	2153711	2153712

4.4 OFETs device fabrication and characterization

Bottom gate, top contact (BG-TC) OFETs devices were fabricated on heavily doped silicon wafers purchased from Si-Mat, (N++/As, resistivity < 0.005 Ω cm) with thermally grown SiO_2 (200 nm) layer. The substrates were cleaned with acetone, ethanol and isopropanol respectively in ultrasound bath, then treated with UV/ozone. Prior to active layer deposition by spin coating, water soluble poly (1-vinyl-1, 2, 4-triazole) (PVT) was spin-coated (2000 rpm for 60 s) onto SiO_2 as passivation layer (thickness of 15 nm) from a solution of 3 mg/ml concentration in water, followed by an annealing process at 80 °C for two hours. Molecules were dissolved in chlorobenzene (CB) at a concentration of 10 mg/ml and were spin-coated (1000 rpm for 90 s) directly on top of PVT in ambient condition, then annealed at 50 °C for 1 h. Prior to 25 nm of active layer deposition by vapour deposition, polystyrene (3 mg/ml in chlorobenzene) was spin coated (2000 rpm, 60s) on top to passivate the surface (thickness of 18 nm). Molecules were evaporated in a thermal evaporator at a base pressure of 1×10^{-6} mbar with a controlled rate of 1 nm /min. MoO_3 (10 nm)/Ag (70 nm) source/drain electrodes were evaporated through a shadow mask at a deposition rate of 10 nm/mins. OFETs channel width is 1 mm, while channel length is 50 µm. The OFETs were characterized using Keithley 4200 semiconductor analyser in a dry nitrogen glove box without exposure to air after the electrode deposition.

4.5 Theoretical calculations

Electronic structure calculations were performed using Gaussian 09.[38] Electronic coupling calculations used geometries of unique molecular pairs taken from the crystal structures. All calculations used the ωB97XD exchange-correlation functional equipped with the 6-311+G(d,p) basis set with a superfine integration grid, and two-electron integral accuracy increased to 10^{-11}.[39-41] Alkyl groups were replaced with methyl to speed up the calculations. Energetic minima were confirmed by calculation and inspection of the vibrational modes, which showed zero imaginary frequencies in all cases. Coupling values were calculated using two different methods (DIPRO[42] and monomer projection[43]), which provided similar values. Mobilities were calculated using a sum-over-neighbours approach using rate constants derived from Marcus theory.[44] Hole transfer electronic couplings for unique molecular pairs extracted from the crystal structures of **4** and **5** are provided in the Supporting Information.

Conflicts of interest

There are no conflicts to declare.

Acknowledgements

The authors thank the CNRS, the University of Angers and the RFI Regional project LUMOMAT (grant to M.M.T., project HEROES). Ingrid Freuze and Sonia Jerjir (University of Angers) are gratefully acknowledged for MS characterization, and

Magali Allain (University of Angers) for help with the X-ray structures. P. H. acknowledges support from the Royal Society of New Zealand for the award of a Marsden Fast-Start and the MacDiarmid Institute. All calculations were performed using the Victoria University of Wellington high performance computing cluster ‘‘Rāpoi’’.

Notes and references

1. W. Jiang, Y. Li and Z. Wang, *Chem. Soc. Rev.*, 2013, **42**, 6113-6127.
2. G. Schweicher, G. Garbay, R. Jouclas, F. Vibert, F. Devaux and Y. H. Geerts, *Adv. Mater.*, 2020, **32**, 1905909.
3. K. Takimiya, S. Shinamura, I. Osaka and E. Miyazaki, *Adv. Mater.*, 2011, **23**, 4347-4370.
4. Y. Yuan, G. Giri, A. L. Ayzner, A. P. Zoombelt, S. C. B. Mannsfeld, J. Chen, D. Nordlund, M. F. Toney, J. Huang and Z. Bao, *Nat. Commun.*, 2014, **5**, 3005.
5. H. Ebata, T. Izawa, E. Miyazaki, K. Takimiya, M. Ikeda, H. Kuwabara and T. Yui, *J. Am. Chem. Soc.*, 2007, **129**, 15732-15733.
6. L. Torsi, G. M. Farinola, F. Marinelli, M. C. Tanese, O. H. Omar, L. Valli, F. Babudri, F. Palmisano, P. G. Zambonin and F. Naso, *Nat. Mater.*, 2008, **7**, 412-417.
7. S. Arnaboldi, T. Benincori, A. Penoni, L. Vaghi, R. Cirilli, S. Abbate, G. Longhi, G. Mazzeo, S. Grecchi, M. Panigati and P. R. Mussini, *Chem. Sci.*, 2019, **10**, 2708-2717.
8. S. Arnaboldi, S. Cauteruccio, S. Grecchi, T. Benincori, M. Marcaccio, A. O. Biroli, G. Longhi, E. Licandro and P. R. Mussini, *Chem. Sci.*, 2019, **10**, 1539-1548.
9. X. Zhang, Y. Zhang, Y. Li, Y. Quan, Y. Cheng and Y. Li, *Chem. Commun.*, 2019, **55**, 9845-9848.
10. Y. Yang, R. C. da Costa, M. J. Fuchter and A. J. Campbell, *Nat. Phot.*, 2013, **7**, 634-638.
11. L. Zhang, I. Song, J. Ahn, M. Han, M. Linares, M. Surin, H.-J. Zhang, J. H. Oh and J. Lin, *Nat. Commun.*, 2021, **12**, 142.
12. V. Kiran, S. P. Mathew, S. R. Cohen, I. Hernández Delgado, J. Lacour and R. Naaman, *Adv. Mater.*, 2016, **28**, 1957-1962.
13. Y. Yang, B. Rice, X. Shi, J. R. Brandt, R. Correa da Costa, G. J. Hedley, D.-M. Smilgies, J. M. Frost, I. D. W. Samuel, A. Otero-de-la-Roza, E. R. Johnson, K. E. Jelfs, J. Nelson, A. J. Campbell and M. J. Fuchter, *ACS Nano*, 2017, **11**, 8329-8338.
14. C. Chen, L. Gao, W. Gao, C. Ge, X. Du, Z. Li, Y. Yang, G. Niu and J. Tang, *Nat. Commun.*, 2019, **10**, 1927.
15. M. A. Khalily, H. Usta, M. Ozdemir, G. Bakan, F. B. Dikecoglu, C. Edwards-Gayle, J. A. Hutchinson, I. W. Hamley, A. Dana and M. O. Guler, *Nanoscale*, 2018, **10**, 9987-9995.
16. O. Kwon, X. Cai, W. Qu, F. Liu, J. Szydłowska, E. Gorecka, M. J. Han, D. K. Yoon, S. Poppe and C. Tschierske, *Adv. Funct. Mater.*, 2021, **31**, 2102271.
17. K. Sumitomo, Y. Sudo, K. Kanazawa, K. Kawabata and K. Takimiya, *Mater. Horiz.*, 2022, **9**, 444-451.
18. K. Niimi, S. Shinamura, I. Osaka, E. Miyazaki and K. Takimiya, *J. Am. Chem. Soc.*, 2011, **133**, 8732-8739.
19. T. Mori, T. Nishimura, T. Yamamoto, I. Doi, E. Miyazaki, I. Osaka and K. Takimiya, *J. Am. Chem. Soc.*, 2013, **135**, 13900-13913.

20. J.-I. Park, J. W. Chung, J.-Y. Kim, J. Lee, J. Y. Jung, B. Koo, B.-L. Lee, S. W. Lee, Y. W. Jin and S. Y. Lee, *J. Am. Chem. Soc.*, 2015, **137**, 12175-12178.
21. H. Ito, T. Yamamoto, N. Yoshimoto, N. Tsushima, H. Muraoka and S. Ogawa, *Heteroat. Chem*, 2013, **24**, 25-35.
22. S. Mu, K. Oniwa, T. Jin, N. Asao, M. Yamashita and S. Takaishi, *Org. Electron.*, 2016, **34**, 23-27.
23. P. Leriche, J.-M. Raimundo, M. Turbiez, V. Monroche, M. Allain, F.-X. Sauvage, J. Roncali, P. Frère and P. J. Skabara, *J. Mater. Chem.*, 2003, **13**, 1324-1332.
24. M.-C. Chen, Y.-J. Chiang, C. Kim, Y.-J. Guo, S.-Y. Chen, Y.-J. Liang, Y.-W. Huang, T.-S. Hu, G.-H. Lee, A. Facchetti and T. J. Marks, *Chem. Commun.*, 2009, **-**, 1846-1848.
25. C. Ruzié, J. Karpinska, A. R. Kennedy and Y. H. Geerts, *J. Org. Chem.*, 2013, **78**, 7741-7748.
26. T. Yamamoto, S. Shinamura, E. Miyazaki and K. Takimiya, *Bull. Chem. Soc. Jpn.*, 2010, **83**, 120-130.
27. M. Abbas, G. Cakmak, N. Tekin, A. Kara, H. Y. Guney, E. Arici and N. S. Sariciftci, *Org. Electron.*, 2011, **12**, 497-503.
28. A. Ablat, A. Kyndiah, G. Houin, T. Y. Alic, L. Hirsch and M. Abbas, *Sci. Rep.*, 2019, **9**, 6685.
29. K. Takimiya, K. Bulgarevich, M. Abbas, S. Horiuchi, T. Ogaki, K. Kawabata and A. Ablat, *Adv. Mater.*, 2021, **33**, 2102914.
30. A. Dieckmann, H. Bässler and P. M. Borsenberger, *J. Chem. Phys.*, 1993, **99**, 8136-8141.
31. D. Hertel and H. Bässler, *ChemPhysChem*, 2008, **9**, 666-688.
32. H. Bürckstümmer, E. V. Tulyakova, M. Deppisch, M. R. Lenze, N. M. Kronenberg, M. Gsänger, M. Stolte, K. Meerholz and F. Würthner, *Angew. Chem. Int. Ed.*, 2011, **50**, 11628-11632.
33. P. Josse, L. Favereau, C. Shen, S. Dabos-Seignon, P. Blanchard, C. Cabanetos and J. Crassous, *Chem. Eur. J.*, 2017, **23**, 6277-6281.
34. M. Chen, J. Li, X. Jiao, X. Yang, W. Wu, C. R. McNeill and X. Gao, *J. Mater. Chem. C*, 2019, **7**, 2659-2665.
35. C. Réthoré, N. Avarvari, E. Canadell, P. Auban-Senzier and M. Fourmigué, *J. Am. Chem. Soc.*, 2005, **127**, 5748-5749.
36. F. Pop, P. Auban-Senzier, A. Frąckowiak, K. Ptaszyński, I. Olejniczak, J. D. Wallis, E. Canadell and N. Avarvari, *J. Am. Chem. Soc.*, 2013, **135**, 17176-17186.
37. S. R. Domingos, K. Martin, N. Avarvari and M. Schnell, *Angew. Chem. Int. Ed.*, 2019, **58**, 11257-11261.
38. Gaussian 09, Revision D.01, M. J. Frisch, G. W. Trucks, H. B. Schlegel, G. E. Scuseria, M. A. Robb, J. R. Cheeseman, G. Scalmani, V. Barone, B. Mennucci, G. A. Petersson, H. Nakatsuji, M. Caricato, X. Li, H. P. Hratchian, A. F. Izmaylov, J. Bloino, G. Zheng, J. L. Sonnenberg, M. Hada, M. Ehara, K. Toyota, R. Fukuda, J. Hasegawa, M. Ishida, T. Nakajima, Y. Honda, O. Kitao, H. Nakai, T. Vreven, J. A. Montgomery, Jr., J. E. Peralta, F. Ogliaro, M. Bearpark, J. J. Heyd, E. Brothers, K. N. Kudin, V. N. Staroverov, T. Keith, R. Kobayashi, J. Normand, K. Raghavachari, A. Rendell, J. C. Burant, S. S. Iyengar, J. Tomasi, M. Cossi, N. Rega, J. M. Millam, M. Klene, J. E. Knox, J. B. Cross, V. Bakken, C. Adamo, J. Jaramillo, R. Gomperts, R. E. Stratmann, O. Yazyev, A. J. Austin, R. Cammi, C. Pomelli, J. W. Ochterski, R. L. Martin, K. Morokuma, V. G. Zakrzewski, G. A. Voth, P. Salvador, J. J. Dannenberg, S. Dapprich, A. D. Daniels, O. Farkas, J. B. Foresman, J. V. Ortiz, J. Cioslowski and D. J. Fox, Gaussian, Inc., Wallingford CT, 2013.
39. J.-D. Chai and M. Head-Gordon, *J. Chem. Phys.*, 2008, **128**, 084106.

40. J.-D. Chai and M. Head-Gordon, *Phys. Chem. Chem. Phys.*, 2008, **10**, 6615-6620.
41. J.-D. Chai and M. Head-Gordon, *J. Chem. Phys.*, 2009, **131**, 174105.
42. B. Baumeier, J. Kirkpatrick and D. Andrienko, *Phys. Chem. Chem. Phys.*, 2010, **12**, 11103-11113.
43. E. F. Valeev, V. Coropceanu, D. A. da Silva Filho, S. Salman and J.-L. Brédas, *J. Am. Chem. Soc.*, 2006, **128**, 9882-9886.
44. A. N. Sokolov, S. Atahan-Evrenk, R. Mondal, H. B. Akkerman, R. S. Sánchez-Carrera, S. Granados-Focil, J. Schrier, S. C. B. Mannsfeld, A. P. Zoombelt, Z. Bao and A. Aspuru-Guzik, *Nat. Commun.*, 2011, **2**, 437.